Supplementary Information (SI) for ChemComm.

This journal is © The Royal Society of Chemistry 2025

Supplementary Information (SI)

Synergistic Effect of A-Site Deficiency and Exsolved Fe Particles in $Sr_{1-x}FeO_{3-\delta}$ Cathodes for Enhanced CO_2 Electroreduction in Solid Oxide Electrolysis Cells

Muhammad Nadeem Khan[b,c], Lingting Ye*[, c,d] and Lizhen Gan*[,a]

[a.] *College of Smart Energy, Shanghai Jiao Tong University, 800 Dongchuan Road, Shanghai 200240, China*
[b.] *School of Mechanical Engineering, Shanghai Jiao Tong University, 800 Dongchuan Road, Shanghai 200240, China*
[c.] *Key Laboratory of Design and Assembly of Functional Nanostructures, Fujian Institute of Research on the Structure of Matter, Chinese Academy of Sciences, Fuzhou 350002, China*
[d.] *Strait Laboratory of Flexible Electronics (SLoFE), Fujian Key Laboratory of Flexible Electronics, Strait Institute of Flexible Electronics (Future Technologies), Fujian Normal University, Fuzhou 350117, China*
* *Correspondence:* ltye@fjnu.edu.cn, ganlizhen@sjtu.edu.cn

1 Experimental

1.1 *Powder synthesis*

Perovskite materials with the composition $Sr_{1-x}FeO_{3-\delta}$ (where x = 0, 0.05, 0.1, 0.15, 0.2) were prepared using the EDTA-citric acid complexation technique[1-3]. Initially, stoichiometric amounts of $Sr(NO_3)_2$ and $Fe(NO_3)_3 \cdot 9H_2O$ were dissolved in distilled water. Chelating agents, citric acid (CA, 99.9%) and ethylenediamine tetraacetic acid (EDTA, 99.9%), were added. The molar ratio of total metal ions to CA to EDTA was kept at 1:2:1. The pH of the solution was adjusted to approximately 7 using an ammonia solution, and the mixture was continuously stirred on a hot plate until a gel was formed. The gel was then heated to 250 °C to trigger combustion. The precursors were pretreated at 210 °C for 10 h, followed by firing at 1100 °C for 7 h to produce the final perovskite materials[4]. The performance of these synthesized perovskite materials in CO_2 electrolysis was assessed using a symmetrical solid oxide electrolysis cell (SOEC) with a $La_{0.9}Sr_{0.1}Ga_{0.8}Mg_{0.2}O_{3-\delta}$ (LSGM) electrolyte. The LSGM electrolyte powder was synthesized using the solid-state method involving the mixing of La_2O_3, $SrCO_3$, MgO, and Ga_2O_3 via ball milling at 300 rpm for 4 h with ethanol as the medium. The mixture was then thermally treated at 960 °C for 6 h in a muffle furnace. Additionally, $Ce_{0.8}Sm_{0.2}O_{2-\delta}$ (SDC) powder was produced using the glycine-nitrate combustion method, with cerium nitrate hexahydrate and samarium oxide as precursors. The pH of the solution was adjusted to 2 by using HNO_3 and $NH_3 \cdot H_2O$. The mixture was heated and stirred at 160 °C until combustion, and the resulting product was calcined in a muffle furnace at 800 °C for 3 h.

1.2. Cell fabrication

A 20 mm-diameter LSGM electrolyte wafer was produced by compressing 0.65 g the LSGM powder at 7 MPa for 10 s using a powder compactor. The compacted wafer was calcined in a muffle furnace at 1400 °C for 10 h to form a dense ceramic electrolyte. For the cathode material preparation, a blend was made by thoroughly mixing 0.65 g of $Sr_{1-x}FeO_{3-\delta}$ (with x values of 0, 0.05, 0.1, 0.15, 0.2), 0.35 g of SDC ($Ce_{0.8}Sm_{0.2}O_{2-\delta}$), 0.2 g of ethyl cellulose ($C_6H_7O_2(OC_2H_5)_x(OH)_{3-x}$) (≥99%), and 0.05 g of tapioca starch $(C_6H_{10}O_5)_n$ (≥99%) in an agate mortar. Approximately 1.0 mL of $C_{10}H_{18}O$ (≥99%) was gradually added to this mixture, which was then ground

further to achieve a uniform slurry. This slurry was applied to both sides of an LSGM wafer and sintered at 1100 °C for 3 h in a muffle furnace to create a three-layer structure. Silver paste was used as the current collector, and silver wires were attached as electrical conductors. The solid oxide electrolysis cell (SOEC) was completed with an effective electrode area of 0.5 cm^2 on one side, followed by heating at 550 °C for 30 minutes to ensure proper adhesion and conductivity.

1.3 Materials characterization

The phase composition of $Sr_{1-x}FeO_{3-\delta}$ (x = 0, 0.05, 0.1, 0.15, 0.2) powders, synthesized through the sol-gel technique, was investigated using X-ray Diffraction (XRD, Rigaku Miniflex600). The microstructure of the electrode was examined using Scanning Electron Microscopy (SEM, Hitachi SU-8010) and energy-dispersive spectroscopy (EDS) to evaluate the size and distribution of Fe nanoparticles. High-Resolution Transmission Electron Microscopy (HRTEM, FEI Tecnai G20F30) provided further insight into the triple-phase boundary (TPB) microstructure, with lattice fringes verifying the particle composition. The valence states of Sr, Fe, and O were determined by XPS (Thermo Fisher EscaLab 250Xi). Electrical conductivity measurements were conducted using a Keithley 2400 source meter via a four-terminal approach. Vacuum Fourier transform infrared spectroscopy (FT-IR, BRUKER Vertex 70V) was employed to monitor the compositional changes during the catalytic process. Thermogravimetric Analysis (TGA, NETZSCH STA 449 F5) was used to determine the relative oxygen content, while Electron Paramagnetic Resonance (EPR, Bruker ELEXSYS E500) was used to quantify the oxygen vacancies. The impact of the modifications on CO_2 adsorption was evaluated using the Brunauer–Emmett–Teller (BET) method with a Micromeritics ASAP 2020 analyzer. Temperature-programmed reduction (TPR) with H_2 and temperature-programmed desorption (TPD) with He were performed using a Micromeritics AutoChem II 2920 instrument to study the reduction and CO_2 adsorption characteristics. The electrochemical properties, including Electrochemical Impedance Spectroscopy (EIS), were assessed using an Electrochemical Workstation (Zahner Zennium). Gas components and concentrations were analyzed via Gas Chromatography (Shimadzu GC 2014), and Raman spectroscopy (Horiba LabRAM HR Evolution) was utilized to characterize carbon deposition during the reaction process.

Samples	O_{latt}/O	O_{abs}/O	O_w/O	O_{abs}/O_{latt}	Fe^{3+}/Fe	Fe^{4+}/Fe
Oxidized $Sr_{0.85}FeO_{3-\delta}$	22.38%	54.75%	22.82%	2.44	66.96%	33.13%
Reduced $Sr_{0.85}FeO_{3-\delta}$	11.98%	83.20%	12.76%	6.94	70.29%	29.69%

Table S1 Surface atomic ratios of the fresh and reduced samples obtained from X-ray photoelectron spectrometer results

XPS data before and after reduction, please explain why no Fe^0 signal was observed?

The absence of an Fe^0 signal in the XPS spectra before and after reduction arises from the intrinsic redox behavior and structural stability of Fe-based perovskites. In these materials, Fe cations are strongly coordinated within FeO_6 octahedra, and reduction primarily proceeds via oxygen vacancy formation accompanied by Fe valence adjustment ($Fe^{4+} \rightarrow Fe^{3+}/Fe^{2+}$) to maintain charge neutrality, rather than by complete reduction to metallic Fe. Thermodynamically, the reduction conditions employed are sufficient to induce non-stoichiometric oxygen loss but insufficient to break the Fe–O bonds required for Fe^0 formation. Furthermore, the reduction was conducted under 5% H_2/Ar atmosphere without strong reducing agents, which further limited the reaction to partial reduction pathways[5,6]. In addition, XPS is a surface-sensitive ex situ technique; any trace metallic Fe that might transiently form during reduction would be highly unstable and readily re-oxidized upon exposure to air during sample transfer, rendering it undetectable. These factors collectively explain the absence of Fe^0 signals in XPS spectra.

Result and Discussion

Fig. S1(a) and **(b)** display the temperature-dependent electrical conductivities of $Sr_{1-x}FeO_{3-\delta}$ (x = 0, 0.05, 0.1, 0.15, 0.2) cathode materials. In **Fig. S1(a & b)**, it is evident that the conductivity of the oxidized $Sr_{1-x}FeO_{3-\delta}$ (x = 0, 0.05, 0.1, 0.15, 0.2) samples initially rises with increasing temperature, followed by a decline. On the other hand, the reduced $Sr_{1-x}FeO_{3-\delta}$ (x = 0, 0.05, 0.1, 0.15, 0.2) samples show a continuous increase in conductivity as the temperature goes up. The oxidized $Sr_{0.85}FeO_{3-\delta}$ reaches a peak conductivity of about 3.64 lnσ S cm^{-1}, while the reduced $Sr_{0.85}FeO_{3-\delta}$ achieves its maximum conductivity of approximately 0.69 lnσ S cm^{-1} in a 5% H_2/Ar atmosphere at 850 °C. The findings underscore the potential of $Sr_{0.85}FeO_{3-\delta}$ as a viable material for cathodes in Solid Oxide Electrolysis Cells (SOEC)[7]. To enhance the conductivity, Samarium-Doped Ceria (SDC) was added to the electrode slurry to achieve an electrode thickness of 20 μm. When reduced at 850 °C, the Fe nanoparticles were evenly dispersed and securely embedded within the $Sr_{0.85}FeO_{3-\delta}$ framework, which prevented clumping and improved stability.

Fig. S1-c illustrates the study of CO_2 chemical adsorption on reduced $Sr_{1-x}FeO_{3-\delta}$ (x = 0, 0.05, 0.1, 0.15, 0.2) samples using FT-IR spectroscopy at a temperature of 850 °C. Prior to this, the samples were fully reduced by treating $Sr_{1-x}FeO_{3-\delta}$ (x = 0, 0.05, 0.1, 0.15, 0.2) in a 5% H_2/Ar reducing atmosphere at 850 °C for 20 hours, as previously outlined. The FT-IR spectra display two distinct absorption bands: one between 2400 and 2300 cm^{-1}, which is typically linked to molecular CO_2, and another between 1500 and 1400 cm^{-1}, indicative of carbonate ions (CO_3^{2-})[8,9]. These findings imply that the CO_2 adsorbed on the surface of $Sr_{1-x}FeO_{3-\delta}$ (x = 0, 0.05, 0.1, 0.15, 0.2) exists in a state that is intermediate between molecular and ionic forms, suggesting strong adsorption[10]. Moreover, the **S1-d's** Raman spectrum reveals that there are no prominent C–C vibrational bands[3,4].

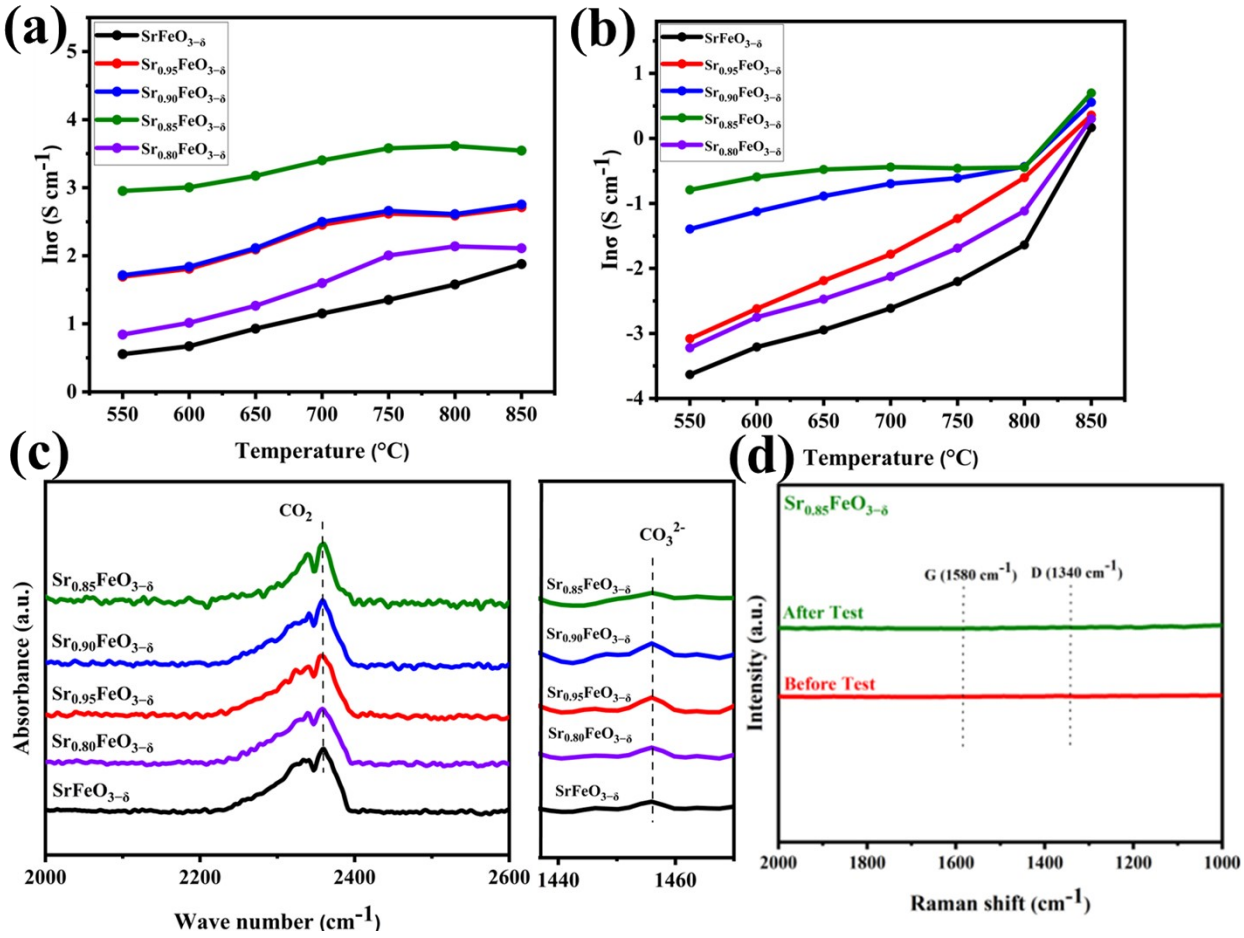

Fig. S1 Conductivity of $Sr_{1-x}FeO_{3-\delta}$ (x = 0, 0.05, 0.1, 0.15, 0.2) samples in (a) air and (b) 5%H_2/95%Ar; (c) Infrared absorption spectra of the reduced $Sr_{1-x}FeO_{3-\delta}$ (x = 0, 0.05, 0.1, 0.15, 0.2); (d) Raman test results of $Sr_{0.85}FeO_{3-\delta}$.

The study examined the formation of oxygen vacancies in $SrFeO_{3-\delta}$ and $Sr_{1-x}FeO_{3-\delta}$ (x = 0, 0.05, 0.1, 0.15, 0.2) samples under high-temperature conditions using thermogravimetric analysis (TGA). A key factor in this process is the reduction of metal ions, particularly in the conversion of Fe^{4+} to Fe^{3+}. This reduction is crucial for generating oxygen vacancies and is represented by Equation (1), which describes the interaction between $SrFeO_{3-\delta}$ and oxygen molecules:

$$O^{x}_{o} + 2Fe^{\bullet} \rightarrow V^{\bullet\bullet} + 2Fe^{\times}_{Fe} + 1/2O_2 \qquad (1).$$

The reduction process led to a decrease in mass, indicating the formation of oxygen vacancies and a simultaneous reduction in p-type charge carriers[11]. **Fig. S2-b** presents the TGA curves for the $SrFeO_{3-\delta}$ and $Sr_{1-x}FeO_{3-\delta}$ (x = 0, 0.05, 0.1, 0.15, 0.2) samples when heated in air. Notably, the $Sr_{0.85}FeO_{3-\delta}$ samples showed a significantly greater mass loss (4.99%) compared to $SrFeO_{3-\delta}$ (2.61%), suggesting that A-site deficiency promotes the formation of oxygen vacancies. These results align with the findings of the thermogravimetric analysis (TGA) and X-ray photoelectron spectroscopy (XPS).

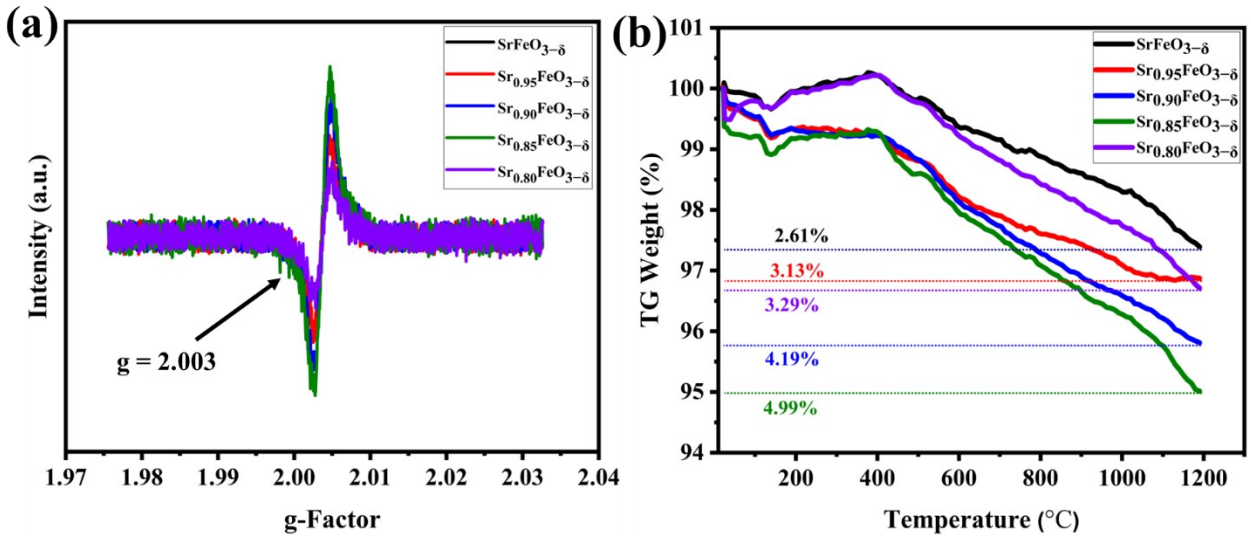

Fig. S2 $Sr_{1-x}FeO_{3-\delta}$ (x = 0, 0.05, 0.1, 0.15, 0.2) samples of (a) EPR analysis; (b) TGA analysis

To evaluate how the A-site deficiency and oxygen vacancies affect the CO_2 adsorption capacity of the sample, CO_2 temperature-programmed desorption (CO_2-TPD) tests were performed, and the results are displayed in **Fig. S3-a**. The peak at lower temperatures (below 220 °C) is linked to the physical adsorption of CO_2, whereas the peak at higher temperatures is associated with chemical adsorption, which is related to the presence of oxygen vacancies and A-site deficiency in the sample. All $Sr_{1-x}FeO_{3-\delta}$ (x = 0, 0.05, 0.1, 0.15, 0.2) samples showed higher desorption peaks across all temperature ranges compared to $SrFeO_{3-\delta}$, suggesting a stronger CO_2 adsorption capability due to the increased concentration of oxygen vacancies. Moreover, a new adsorption peak at 667 °C was observed for $Sr_{0.85}FeO_{3-\delta}$ compared to $SrFeO_{3-\delta}$, which might be linked to oxygen vacancies caused by charge imbalance due to A-site deficiency[12,13].

To ascertain the impact of Fe nanoparticles and A-site deficiency on CO_2 adsorption, CO_2-BET tests were carried out on $SrFeO_{3-\delta}$ and $Sr_{0.85}FeO_{3-\delta}$, respectively. **Fig. S3-b** shows that $Sr_{0.85}FeO_{3-\delta}$ achieved a superior CO_2 adsorption capacity and exhibited more rapid adsorption and desorption rates under the same experimental conditions. Furthermore, the adsorption and desorption curve for $SrFeO_{3-\delta}$ remained partially open, suggesting the formation of carbon on the surface post-CO_2 adsorption. In contrast, the curve for $Sr_{0.85}FeO_{3-\delta}$ was completely closed, indicating no carbon accumulation[14].

The peaks emerging in **Fig. S3-c** between 400 °C to 600 °C can be linked to the gradual reduction process from Fe^{4+}/Fe^{3+} to Fe^{3+}/Fe^{2+}. Further reduction from Fe^{2+} to metallic Fe^0 generally occurs at 600–700 °C and 700–800 °C intervals[15]. Moreover, the peak observed above 800 °C was probably related to the reduction of the bulk $SrFeO_{3-\delta}$ material[16].

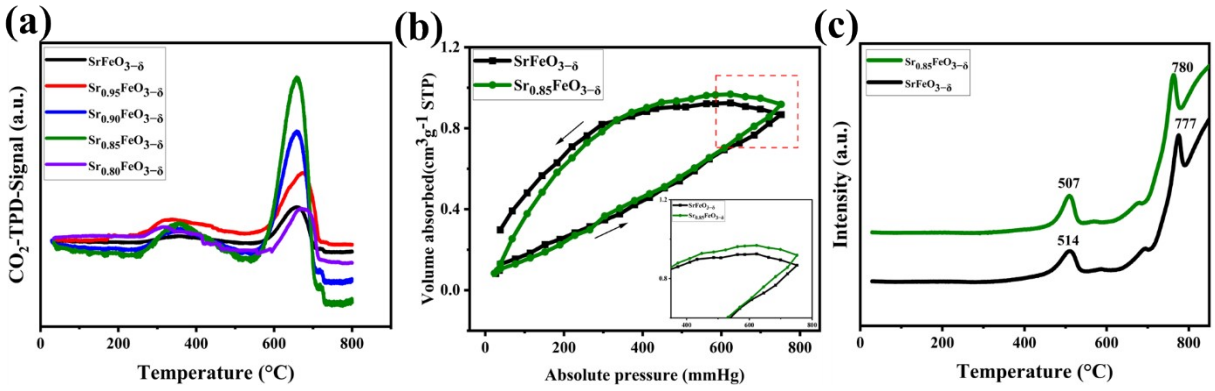

Fig. S3 $Sr_{1-x}FeO_{3-\delta}$ (x = 0, 0.05, 0.1, 0.15, 0.2) samples of (a) CO_2- TPD analysis; (b) CO_2-BET test (c) H_2-TPR test

Fig. S4 illustrates the AC impedance spectra for $SrFeO_{3-\delta}$ and $Sr_{1-x}FeO_{3-\delta}$ samples with varying strontium concentrations (x = 0, 0.05, 0.1, 0.15, 0.2) under different voltages (1.2, 1.4, 1.6, and 1.8 V). The $Sr_{0.85}FeO_{3-\delta}$ sample showed an ohmic resistance of 0.62 $\Omega \cdot cm^{-2}$ and a polarization impedance of 0.16 $\Omega \cdot cm^{-2}$ at 1.8 V, which are notably lower than those achieved through conventional hydrogen reduction techniques. As the voltage increased, the polarization resistance decreased, indicating that higher voltages improved the electrode activation and boosted the efficiency of the electrochemical reaction. The resistances of the compounds were similar, owing to their comparable structural characteristics. However, the $Sr_{1-x}FeO_{3-\delta}$ samples exhibited lower resistance than $SrFeO_{3-\delta}$, implying that the spontaneous formation of Fe nanoparticles and A-site deficiency led to a greater number of active reaction sites. These results underscore the importance of voltage-induced Fe nanoparticle formation on the oxide surface in enhancing the electrochemical performance of solid oxide electrolysis cells (SOEC).

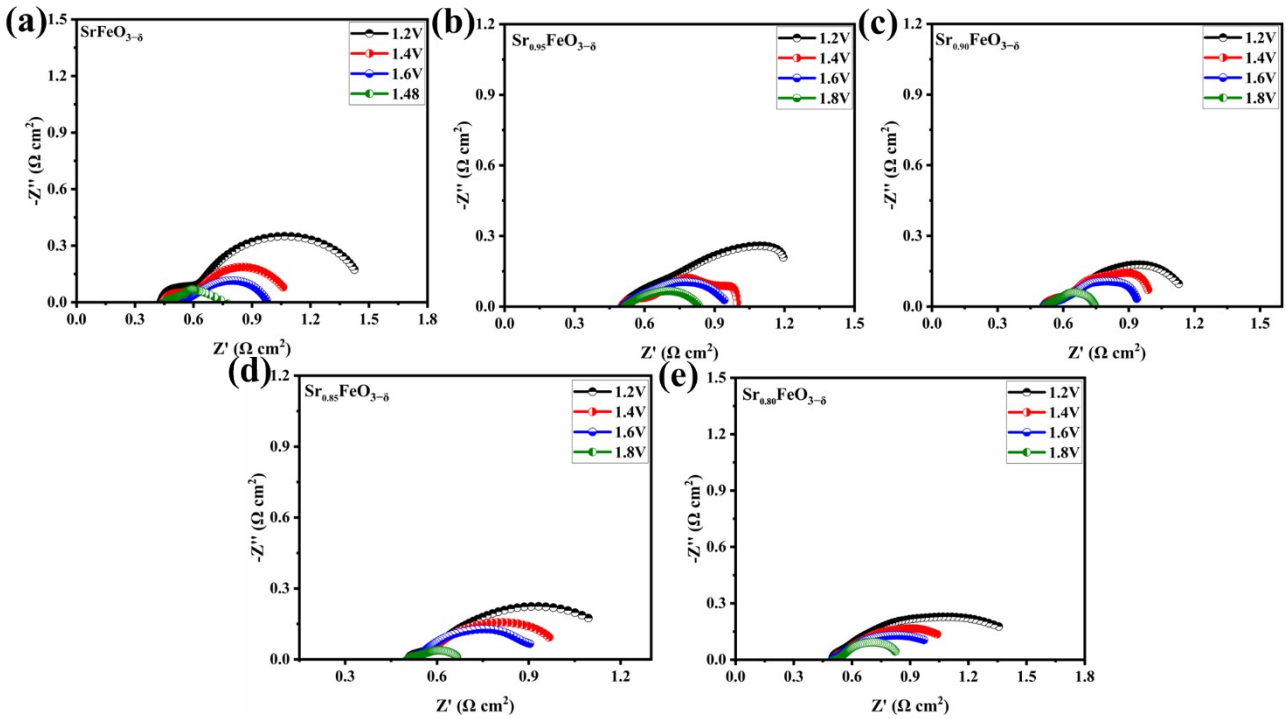

Fig. S4 AC impedance based on (a) $SrFeO_{3-\delta}$; (b) $Sr_{0.95}FeO_{3-\delta}$; (c) $Sr_{0.90}FeO_{3-\delta}$; (d) $Sr_{0.85}FeO_{3-\delta}$; (e) $Sr_{0.80}FeO_{3-\delta}$ in CO_2 atmosphere.

References

[1] D. Huan, L. Zhang, K. Zhu, X. Li, B. Zhang, J. Shi, R. Peng and C. Xia, *Sep. Purif. Technol.*, 2022, **290**, 120843.
[2] H. Lu, D. Wu, Y. Gu, W. Sun, X. Yang, W. Li, H. Shuai and X. Zhao, *Chem. Commun.*, 2023, **59**, 14149–14152.
[3] L. Zhang, W. Sun, C. Xu, R. Ren, X. Yang, J. Qiao, Z. Wang, S. Zhen and K. Sun, *Appl. Catal. B: Environ.*, 2022, **317**, 121754.
[4] M. N. Khan, L. Ye and K. Xie, *Int. J. Hydrogen Energy*, 2024, **93**, 1353–1362.
[5] G. Fang, K. Liu, M. Fan, J. Xian, Z. Wu, L. Wei, H. Tian, H. Jiang, W. Xu, H. Jin and J. Wan, *Carbon Neutralization*, 2023, **2**, 709–720.
[6] Y. Zhou, Z. Zhou, J. Sun, L. Liu, F. Luo, G. Xu and M. Xu, *EcoMat*, 2023, **5**, e12347.
[7] C. Zhu, S. Hou, L. Hou and K. Xie, *Int. J. Hydrogen Energy*, 2018.
[8] M. O. Yusuf, *Appl. Sci.*, 2023, **13**, 3353.
[9] R. T. So, N. E. Blair and A. L. Masterson, *Environ. Chem. Lett.*, 2020, **18**, 1725–1730.
[10] L. Ye, M. Zhang, P. Huang, G. Guo, M. Hong, C. Li, J. T. S. Irvine and K. Xie, *Nat. Commun.*, 2017, **8**, 14785.
[11] Y. Li, Y. Li, Y. Wan, Y. Xie, J. Zhu, H. Pan, X. Zheng and C. Xia, *Adv. Energy Mater.*, 2019, **9**, 1803156.
[12] S. Hu, L. Zhang, H. Liu, Z. Cao, W. Yu, X. Zhu and W. Yang, *J. Power Sources*, 2019, **443**, 227268.
[13] Y. Tian, L. Zhang, Y. Liu, L. Jia, J. Yang, B. Chi, J. Pu and J. Li, *J. Mater. Chem. A*, 2019, **7**, 6395–6400.
[14] X. Gao, L. Ye and K. Xie, *Fuel*, 2024, **371**, 131959.
[15] J. Zieliński, I. Zglinicka, L. Znak and Z. Kaszkur, *Appl. Catal. A: Gen.*, 2010, **381**, 191–196.
[16] M. Wu, H. Yu, J. Ni and C. Ni, *J. Power Sources*, 2022, **552**, 232266.